Design of Low-Power Electronic Circuits & Systems for Point of Care Healthcare Applications

Thesis submitted in partial fulfilment
of the requirements for the degree of

*(Master of Science in **Electronics and Communication Engineering** by Research)*

by

Deeksha
2022702001
deeksha.2022@research.iiit.ac.in

International Institute of Information Technology
Hyderabad - 500 032, INDIA
June 2024

International Institute of Information Technology
Hyderabad, India

CERTIFICATE

It is certified that the work contained in this thesis, titled ***"Design of Low-Power Electronic Circuits & Systems for Point of Care Healthcare Applications"*** by Deeksha, has been carried out under my supervision and is not submitted elsewhere for a degree.

Date

Advisor : Dr. Abhishek Srivastava.

To the Past, Present and Future

Acknowledgments

Completing this Master's thesis has been a trans-formative journey, and I owe a profound debt of gratitude to many who have supported me along the way.

I must first acknowledge the tireless support and guidance of my thesis advisor, **Dr. Abhishek Srivastava**. His expertise and mentorship were crucial to my research and personal growth during this project. Dr. Srivastava's enthusiasm and rigorous standards pushed me to excel, and for that, I am truly grateful.

My family deserves special thanks for their love and encouragement. They have been my emotional bedrock and their unwavering support has been a constant throughout this endeavor. Their belief in my potential has been a source of motivation and resilience.

I am also grateful to my lab-mates, **Arpit Sahani, Srikar Somanchi**, **Narahari N Moudhgalya**, **Anushka Tripathi**, **Ishan Acharrya**, and **Pranjal Mahajan**, for their friendship and collaboration. Sharing this journey with them has not only eased the rigors of research but has also enriched my experience immeasurably.

Lastly, I thank the staff and faculty at IIIT Hyderabad whose support systems and resources were indispensable. Their assistance in navigating administrative and academic requirements allowed me to focus on my research with minimal distractions.

This achievement is not mine alone, and these acknowledgements are but a small token of my appreciation for a large collective effort. Thank you all for being part of my academic adventure.

Abstract

The thesis entitled ”Design of Low-Power Electronic Circuits & Systems for Point of Care Healthcare Applications” focuses on the development of a cutting-edge point of care device tailored for deployment in remote and resource-constrained settings. The impetus for this project stems from the urgent need to extend quality healthcare services in areas where conventional, cumbersome, and expensive medical equipment is untenable.

Engineered for efficiency and ease of use, the device is characterized by its low power consumption and portability, making it well-suited for environments with sparse access to electrical power and established medical facilities. The core technology utilizes Electrical Impedance Spectroscopy (EIS) integrated with vital signs monitoring to detect physiological changes indicative of health conditions that require immediate medical attention. This dual functionality not only enables the early detection of critical health issues but also promotes timely medical interventions, significantly enhancing patient outcomes.

This research further encompasses the innovative design of an active high pass filter within the analog baseband chain of the device’s integrated circuit. These components are specifically tailored for use in Frequency Modulated Continuous Wave (FMCW) radar systems, which form part of the receiver design to accurately detect heart and respiratory rates.

Comprehensive evaluation of the device throughout the research confirms its effectiveness in meeting the healthcare delivery needs of isolated regions. The findings highlight the transformative potential of such devices in improving healthcare accessibility and efficacy across underserved populations. This device emerges as a vital instrument in the global initiative to enhance healthcare delivery, demonstrating significant implications for the future of remote medical practices and technology-driven health interventions.

Contents

List of Figures

List of Tables

Chapter 1

Introduction

The integration of electronic systems into healthcare applications has revolutionized the way medical care is delivered, especially in remote and resource-limited settings. The demand for portable, low-cost, and efficient diagnostic tools has significantly increased, driven by the global need to improve access to medical services and reduce healthcare disparities. This thesis, titled ”Design of Low-Power Electronic Circuits & Systems for Point of Care Applications in Remote Healthcare,” presents the development of a novel point of care device designed to meet these challenges.

1.1 Background and Motivation

Traditional healthcare diagnostic devices, while effective, often fail to serve the populations in remote areas due to their cost, complexity, and power requirements. The advent of point-of-care (POC) technologies has the potential to bridge this gap by enabling early detection of diseases and conditions with compact, easy-to-use devices. Electrochemical Impedance Spectroscopy (EIS) and other biosensing technologies are particularly promising due to their applicability in non-invasive and continuous monitoring systems. However, the integration of such technologies into user-friendly, portable devices suitable for field deployment remains a significant challenge.

1.2 Objectives

The primary objective of this research is to design and implement a series of electronic circuits and systems that enhance the functionality and usability of POC devices in healthcare. These include a biosensor circuit for impedance measurement, a portable integrated system for rapid health assessment, and a novel filter design to improve signal processing capabilities in these devices.

1.3 Contributions

The contributions of this thesis are threefold:

1. The development and implementation of a biosensor circuit using Electrochemical Impedance Spectroscopy (EIS), optimized for healthcare applications, and tested with biological samples such as yeast and lactobacillus using a gold Interdigitated Electrode (IDE) biosensor.

2. The design and testing of a low-cost, portable, integrated 'Go/No-Go' system, named RESPIRE, which demonstrates the integration of various sensors within a cohesive unit, along with the design and fabrication of its associated printed circuit board (PCB) and 3D-printed enclosures.

3. The innovative design of a low-frequency active high pass filter, exploring various topologies and providing comparative performance results, thus contributing to the overall enhancement of signal processing within biomedical applications.

1.4 Structure of the Thesis

This thesis is structured into several chapters, each focusing on a distinct aspect of the research and development conducted. The chapters are outlined below:

1. **Chapter 2: Development of Integrated Microbial Detection System with Fabrication and Evaluation of ZnO Nanorods-Based Biosensor**
   This chapter delves into the development of a bio sensor and associated circuitry tailored for the detection of microorganisms. It provides insights into the design and implementation of the sensor technology aimed at detecting biological entities with portable devices.

2. **Chapter 3: Healthcare System for Respiratory Disease Detection**
   Chapter 3 provides detailed information regarding the development of a healthcare system engineered to detect various respiratory diseases. It outlines the methodologies employed and the technological solutions devised to enable accurate and efficient disease detection.

3. **Chapter 4: Design and Analysis of Active High Pass Filter Topology for Low-Frequency Noise suppression in Signal Processing Applications**
   This chapter presents a methodology for designing an active high pass filter tailored to filter out DC offset and spillover effects. The efficacy of the designed circuit is validated through post-layout simulations conducted using TSMC 65nm CMOS technology. It provides a comprehensive overview of the design process and simulation results.

Each chapter contributes unique insights and advancements to the field, collectively forming a comprehensive body of work aimed at addressing significant challenges and advancing technological solutions in their respective domains.

Chapter 2

Development of Integrated Microbial Detection System with Fabrication and Evaluation of ZnO Nanorods-Based Biosensor

2.1 Introduction

Detecting micro-organisms is essential for maintaining human health, protecting environmental integrity, and ensuring industrial process efficiency. The considerable influence of micro-organisms in various aspects of life emphasizes the need for effective and reliable detection methods. The absence of such methods can lead to delayed disease diagnosis and treatment, inadequate response to health crises, and negative impacts on both the environment and industrial operations. Therefore, the implementation of adept detection technologies is vital for the timely and accurate identification of micro-organisms.

Impedance spectroscopy has proven to be an effective technique and has received significant attention across various scientific domains for its capability to monitor and analyze the electrical properties of biological samples. For instance, A. Soley et al. explored the use of impedance spectroscopy for yeast growth monitoring with a specific type of impedance analyzer, demonstrating the potential of this technique [1]. Despite its effectiveness, the lack of portability of these systems limits their applications in field settings. Further investigations, such as those by Borgohain [2], have introduced different biosensing solutions, yet they face challenges related to error rates and high costs, which impede their widespread adoption and necessitate advancements for practical use.

To overcome these challenges, this thesis presents a novel approach that involves a Zinc Oxide (ZnO) nanorods-based, cost-effective, and portable integrated system for micro-organism detection using electrochemical impedance spectroscopy (EIS). This approach leverages innovative material choices and design techniques including the development of high-yield ZnO nanorods and their incorporation into a sensor system. The system's effectiveness is validated through comprehensive testing methodologies, including scanning electron microscopy. This research showcases the system's capabilities through experimental results focused on the detection of yeast, demonstrating its utility and effectiveness for broader biological applications. The selection of ZnO nanorods is motivated by their biocompatibility, substantial chemical and thermal stability, and adjustable properties, which are crucial for sensitive and specific biosensing applications [3, 4]. The subsequent sections will detail the methodology and experimental outcomes, providing insights into the potential of this innovative detection system for practical applications in biomedical sensing and beyond.

2.2 Electrochemical Bio detection

Streptococcus pneumonia can be detected using various biosensing techniques, such as Polymerase Chain Reaction (PCR), Surface Plasmonic Resonance (SPR), and Antibody-based electrochemical sensors[5, 6, 7]. Among the different techniques, electrochemical sensors boast affordability, user-friendly operation, portability, and swift detection capabilities. Electrochemical biosensors utilize the interaction between an electrochemical transducer (probe) and biological analytes such as proteins, DNA, or microorganisms to observe impedance changes. One of the detection methods, Electrochemical Impedance Spectroscopy (EIS), enables us to get the target's impedance at different frequencies with a single scan[8]. Typically, EIS is performed using a 3-electrode system, which is simplified using an Interdigitated electrode (IDE) to make it more suitable for point-of-care applications[9]. Metal oxide nanorods were fabricated on IDE to promote chemical interactions and biosensor sensitivity, as they offer a higher surface-to-volume ratio. After literature reviewing, zinc oxide (ZnO) emerged as the preferred choice due to its high sensitivity and easy customization for specific bacterial[10, 11]. The impedance of ZnO nanorods-based sensors change when there bacteria in the solution. Due to presence of bacteria, the impedance changes which indicate the presence or absence of pneumonia bacteria. In this section, we have demonstrated a portable electrochemical biosensing system that uses EIS and IDE. ZnO nanorods are grown on IDE to increase the chemical interaction. A Python script was used to estimate weight and determine the percentage of bacteria in a sample.

2.2.1 IDE Design and Simulation

Impedance characterization of the IDE was conducted to ascertain the frequency range of the biosensing system. Fig. 2.1(a) and 2.1(b) illustrate the IDE and its corresponding analytical model, respectively. The relation between the dimensions of an IDE and its impedance parameters has been analysed in [12].

$$Resistance\ of\ solution : R_{sol} = \frac{K_{cell}}{\sigma_{sol}} \tag{2.1}$$

$$Capacitance\ of\ solution : C_{sol} = \frac{\epsilon_0 \epsilon_{rsol}}{K_{cell}} \tag{2.2}$$

Here, σ_{sol} and ϵ_{rsol} represent the solution's conductivity and relative permittivity, respectively. K_{cell} mathematically represents the impact of IDE dimensions on each component of the equivalent model and can be defined by equation (2.3).

$$K_{cell} = \frac{2}{(N-1)L} \times \frac{K(k)}{K(\sqrt{1-k^2})} \tag{2.3}$$

where, $K(k)$ and k are as given by equation. (2.4) and equation. (2.5), respectively. N represents the number of fingers, while W, S, and L represent the width, spacing, and length of fingers.

$$K(k) = \int_0^1 \frac{1}{\sqrt{(1-t^2)(1-k^2t^2)}} dt \tag{2.4}$$

$$k = \cos(\frac{\pi}{2} \times \frac{S}{S+2W}) \tag{2.5}$$

In Fig. 2.1(b), C_{dl} arising from ion accumulation at the electrodes and relies on the electrode's contact area with the solution. C_{dl} can be expressed as equation. (2.6).

$$C_{dl} = 0.5 \times W \times N \times L \times C_{stern,surface} \tag{2.6}$$

For planar electrodes C_{dl} can be approximated as directly proportional to the Stern layer characteristic capacitance, typically falling within the range of 10-20 µF/cm^2[12]. In Fig. 2.1(c), the impedance magnitude and phase are presented for varying values of the finger width (W) when the IDE is submerged in deionized (DI) water. The anticipated resistance of the solution lies within the range of 30 - 35 kΩ. An increase in the finger width (W) correlates with a reduction in the lower dominant frequency of the solution resistance. In Fig. 2.1(c), phase plot shows that resistance will be the dominant factor across the selected frequency range. This frequency range is of paramount significance for the accurate detection of variations in microorganism concentration, as microorganism directly influences the resistance of the solution[13].

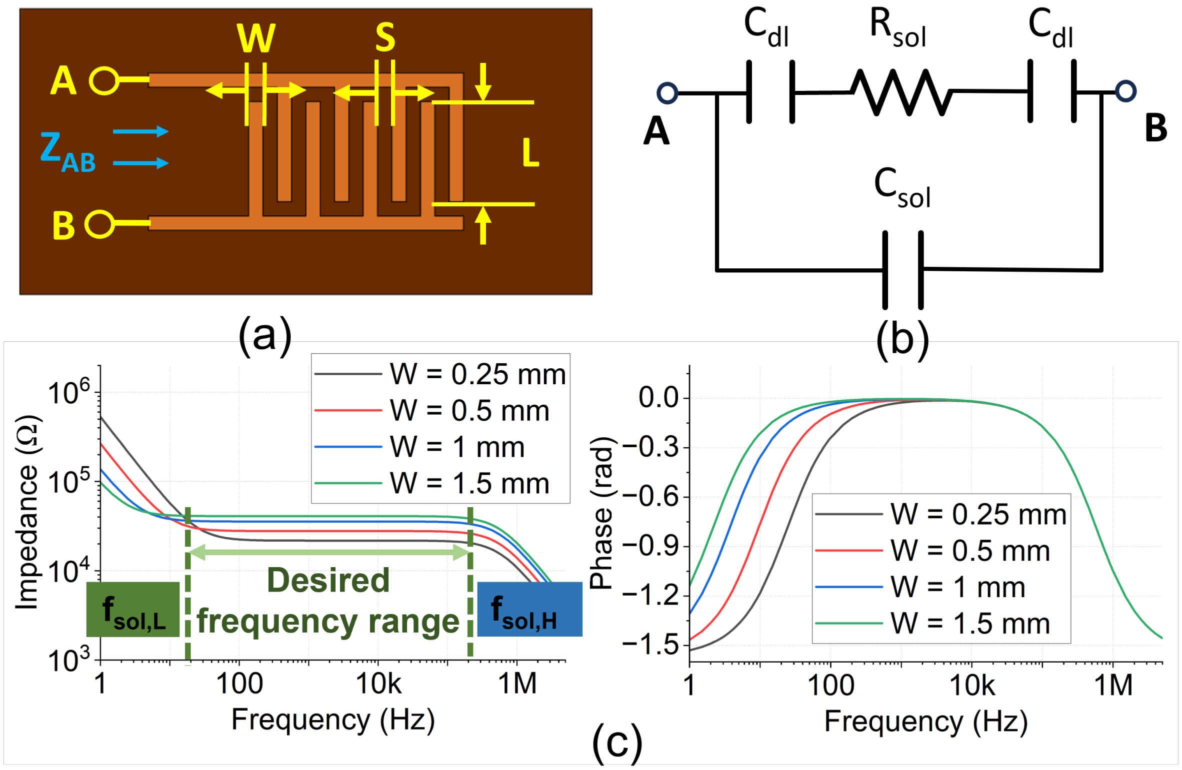

Figure 2.1: (a) IDE design. W, S and L are width, spacing between finger and length of fingers respectively (b) Equivalent model for IDE in (a) when immersed in a solution (c) Impedance and phase of IDE wrt the frequency for different width (W) of electrode

2.2.2 ZnO Nanorods Fabrication

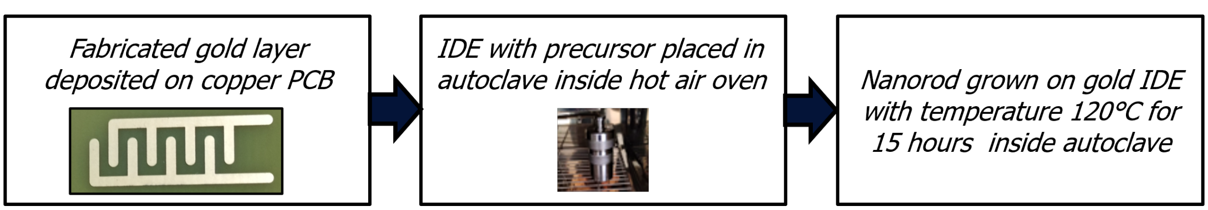

Figure 2.2: Flow chart of ZnO nanorod based IDE fabrication

To enhance the sensitivity and stability of the IDE sensor, ZnO nanorods have been synthesized as a sensing layer over the IDE making them ideal for precise and rapid detection. The fabrication process of ZnO nanorods comprises a two-step procedure. Initially, a seeding layer of ZnO is applied to the Interdigitated Electrode (IDE), succeeded by the growth of nanorods on this seeded layer. We tried fabricating ZnO nanorods on Copper IDE but encountered challenges due to nonuniform seed layer formation. Fig. 2.2 depicts the steps for ZnO nanorods growth. In response, a gold layer was investigated as a more promising seeding layer for optimal ZnO nanorod growth[14, 15]. Utilizing a hydrothermal autoclave reactor further refined growth conditions, ensuring complete coverage. Indepth fabrication has been reported elsewhere[12]. Field-emission scanning electron microscopy (FESEM) was employed for visualization. Experimental results indicated that a concentration of 25mM yielded full nanorod coverage as depicted in Fig. 2.3(a). Additional details on nanorod lengths at various substrate types and concentrations are presented in Table 2.1, providing a comprehensive overview of the observed nanorod development. In the absence of autoclave treatment, observations reveal concentrations of Zn and O, although limited to specific regions of the IDE. Complete coverage has not been attained. Conversely, autoclave treatment achieves full coverage. Fig. 2.3(b) depicts the EDX spectrum of the sensor. Fig. 2.3(c) depicts that the Au substrate, subjected to autoclave treatment, exhibits an increase in Zn and O concentration form 10.87, 10.75 to 49.72, 33.11 respectively.

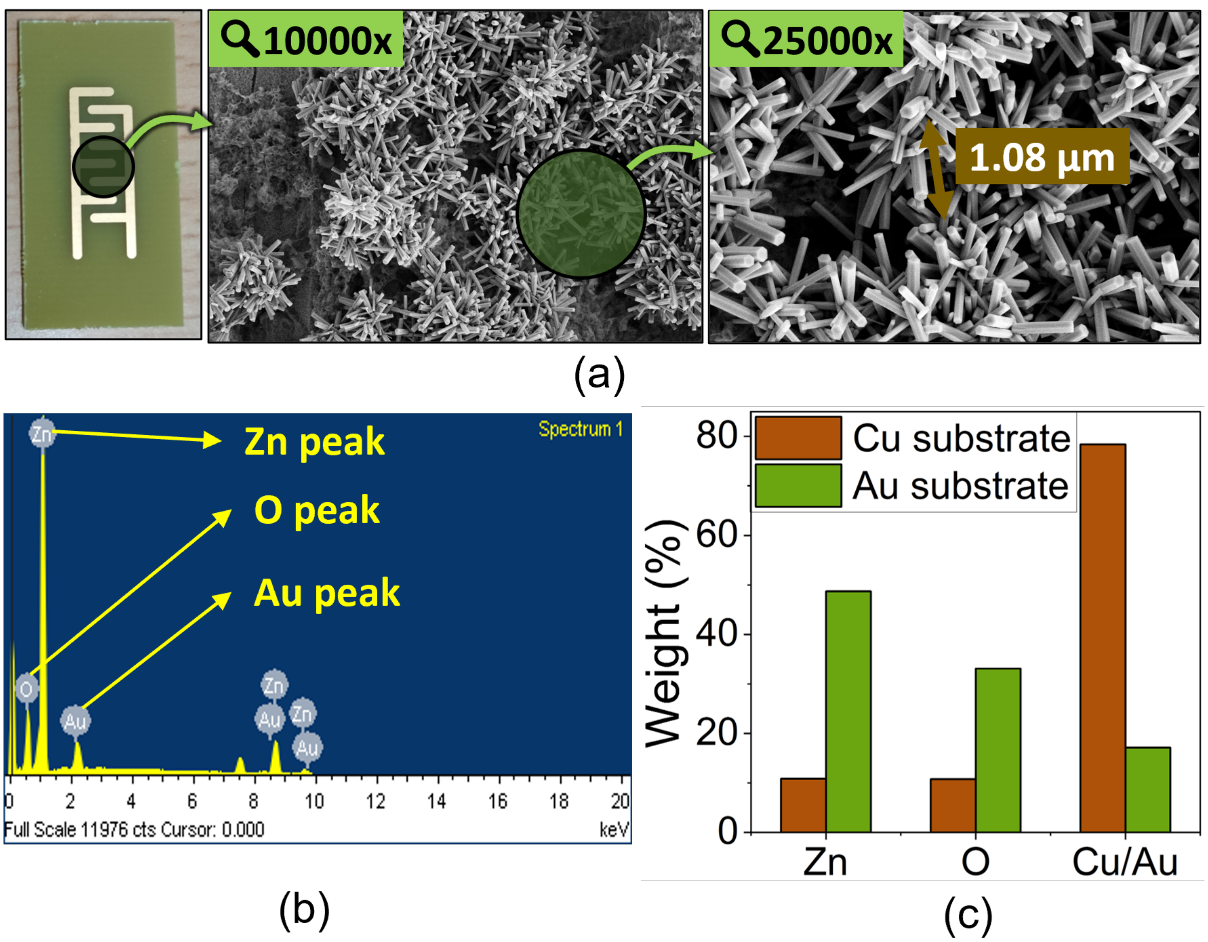

Figure 2.3: (a) Nanorod developed on gold IDE (b) EDX spectrum for ZnO nanorods grown on Au substrate (c) Elemental analysis results of ZnO nanorod on copper and gold IDE

Table 2.1: Nanorod lengths for different substrate and precursor concentrations

Substrate	**Conc. [mM]**	**Length [μm]**	**Coverage**
Cu	20	8.379	Partial
Cu	40	5.924	Partial
Cu	100	3.834	Partial
Au	25	6.451	Full

The gold IDE is subjected to preheating (at 150°C) in hot air oven prior to the growth process inside the hydrothermal autoclave reactor. Following the preheating step, IDE is subjected to same procedure as autoclaving at 120°C for ZnO nanorods growth. The examination of the resulting nanorod growth patterns reveals partial growth. In certain regions, well-shaped nanorods are observed, indicating successful nucleation and growth. However, in other areas, no nanorods growth has been observed. This is due to the maximum temperature tolerance ($<$ 170°C) of the FR4 substrate. Heating beyond this limit causes pores to form over the gold-plated area, leading to insufficient seed layer availability for ZnO nanorod growth. So, preheating to improve nanorods alignment has been eliminated as it proves ineffective. The coverage and average length of nanorods has been summarized in Table 2.1.

2.3 Impedance Measurement:

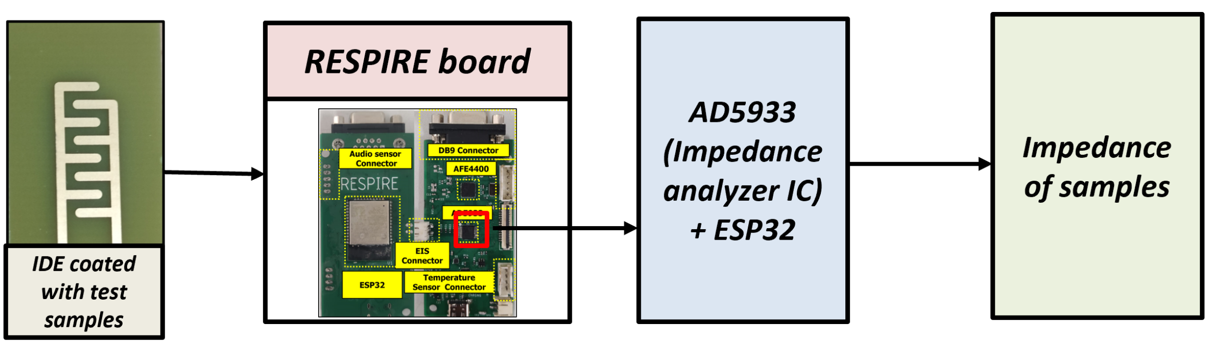

Figure 2.4: Impedance measurement flow chart for biosensor IDE

Electrochemical impedance spectroscopy (EIS) is a powerful analytical technique used to study the electrical properties of electrochemical systems. It involves applying a small amplitude sinusoidal voltage signal across a cell or device and measuring the resulting current response. By varying the frequency of the applied signal over a wide range, EIS can provide detailed information about the electrical behavior of the system under investigation.

The EIS circuit is a key component in performing EIS measurements. It typically consists of the following elements:

- **Impedance Analyzer IC**: An impedance analyzer IC, such as the AD5933 is often used to generate the sinusoidal voltage signal and measure the resulting current response. These ICs offer high precision and flexibility in controlling the frequency and amplitude of the applied signal, making them ideal for EIS applications.

- **Reference and Sense Resistors**: These resistors are used to measure the current passing through the electrochemical cell. The sense resistor is placed in series with the cell, while the reference resistor provides a known reference point for the measurement.

- **Voltage Amplifier**: In some EIS circuits, a voltage amplifier may be used to boost the output voltage of the impedance analyzer IC, particularly if the impedance of the system under test is high or if signal conditioning is required.

- **Signal Conditioning Components**: These components, such as filters and amplifiers, may be used to condition the input and output signals to optimize the measurement accuracy and signal-to-noise ratio.

- **Data Acquisition System**: A data acquisition system, typically connected to a computer, is used to record and analyze the measured impedance data. This system may include analog-to-digital converters (ADCs) for digitizing the measured signals and software for data analysis.

To analyze the impedance data acquired from the biosensor, we employ an AD5933 impedance analyzer IC. This IC is specifically designed to measure impedance values within a wide range, from 1 kOhm to 10 MOhm, across frequencies spanning from 1 Hz to 100 kHz. The biosensor is prepared by coating samples of yeast and lactobacillus onto a substrate comprising ZnO nanorods. As the biological samples interact with the biosensor surface, changes in impedance occur, which are meticulously noted and recorded.

To validate the accuracy of the impedance measurements obtained from the biosensor, we conduct a comparative analysis with a Vector Network Analyzer (VNA). By comparing the impedance data obtained from both the biosensor and the VNA, we can ensure the reliability and precision of our measurements.

Furthermore, in subsequent chapters, we delve into detailed simulation results obtained from the RESPIRE prototype. These results provide comprehensive insights into the performance and capabilities of our proposed device in comparison to conventional impedance measurement techniques. Through these analyses, we aim to demonstrate the effectiveness and potential applications of our biosensor technology in various biomedical and diagnostic scenarios.

Chapter 3

Healthcare System for Respiratory Disease Detection

3.1 Introduction

Global mortality rate has been on the rise due to inadequate access to timely medical care. Early detection of illnesses is crucial in addressing this issue. Respiratory diseases are a leading cause of morbidity and mortality globally, with significant economic and societal burdens. They affect individuals of all ages, from infants to the elderly, and can be exacerbated by factors such as environmental pollution, tobacco smoke, occupational hazards, and genetic predispositions. These diseases can manifest in various forms, ranging from mild respiratory infections to chronic conditions with debilitating effects. Common respiratory illnesses such as asthma, chronic obstructive pulmonary disease (COPD), pneumonia, bronchitis, influenza have been a known disease throughout history [16]. Despite its long history, these diseases remain a major public health concern today, with millions of cases resulting in hospitalization and death around the world. Global Burden of Disease study found that chronic respiratory diseases were the third leading cause of death in 2019, responsible for 4.0 million deaths globally, with a prevalence of 454.6 million cases. The burden of chronic respiratory diseases has increased by 28.5% and 39.8% in terms of total deaths and prevalence, respectively, from 1990 to 2019[17]. The main factor contributing to the high mortality rate is the lack of reliable and rapid diagnostic facilities for early detection.

Various devices used in the detection of respiratory diseases include pulse oximeters, spirometers, peak flow meters, electrocardiograms (ECG or EKG), chest X-rays, and computerized tomography (CT) scans[18, 19]. However, their readings can be influenced by various factors and must be interpreted within the patient's overall clinical context. The high cost, cumbersome nature of equipment, and reliance on human perception contribute to the potential for inaccuracies and errors in diagnosis, making the diagnostic process costly. Furthermore, the lack of portability in current devices restricts their usage to specific clinical settings, limiting their accessibility and utility in scenarios where immediate diagnosis or monitoring is necessary outside of traditional healthcare facilities. In this paper, we propose a device named RESPIRE (Rapid Examination System for Pulmonary Infections and Respiratory Exacerbation) to address these challenges. RESPIRE incorporates several innovative features to revolutionize the detection and monitoring of respiratory diseases:

1. **ZnO Nanorod-Based Biosensor:** RESPIRE features a ZnO nanorod-based biosensor with exceptional sensitivity, enabling it to differentiate between various respiratory disease samples with high accuracy and specificity.

2. **Deep Learning-Based Lung Sound Classification:** Utilizing advanced deep learning algorithms, RESPIRE captures audio data, filters out noise, and classifies lung sounds. This innovative approach enhances diagnostic capabilities by providing additional insights into respiratory conditions.

3. **Multifunctionality:** In addition to respiratory parameters, RESPIRE measures vital signs such as heart rate, SpO_2, and temperature, offering a comprehensive assessment of the patient's condition in a single device.

4. **Embedded Platform Integration:** RESPIRE integrates audio capture, pulse oximetry, and temperature sensing functionalities onto a single embedded platform, enhancing user convenience and reducing the need for multiple devices.

5. **Wireless Connectivity:** With built-in WiFi connectivity, RESPIRE enables seamless wireless communication, facilitating data transmission and remote monitoring for enhanced patient care.

The outline of the paper is as follows: Section 3.2 presents the architecture of RESPIRE device, offering a detailed overview of its design and functionality. Section 3.3 focuses on the biosensor design and fabrication. It provides weight estimation model to detect bacterial concentration. Additionally, methods to increase the biosensor's specificity and selectivity are proposed. The measurement and analysis of vital physiological parameters, such as body temperature, heart rate, and blood oxygen levels, analysis of lung sounds are explored in Section 3.4. In Section 3.5, the hardware implementation details of RESPIRE device are outlined, including the components and technologies utilized. The results obtained from the device's operation and performance are thoroughly analyzed in Section 4.5. Finally, Section 4.6 provides a conclusive discussion, summarizing the key findings, insights, and implications of the research study.

3.2 Architecture

Architecture of RESPIRE is depicted in Fig. 3.1. The system comprises two modules: 1. Sense module 2. Core module.

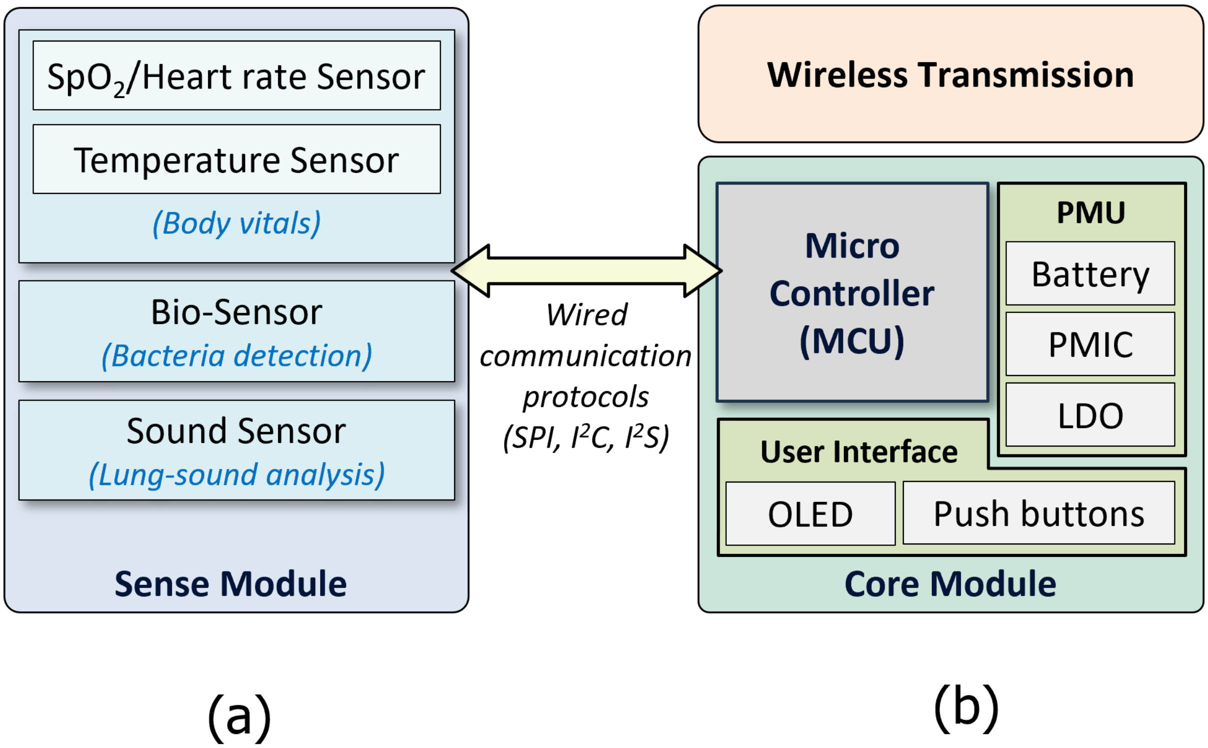

Figure 3.1: Architecture of proposed RESPIRE device (a) Sense Module (b) Core Module

3.2.0.0.1 Sense Module : The Sense module (Fig. 3.1(a)) integrates various sensor blocks to gather information on key biomarkers crucial for respiratory diseases. These biomarkers are selected based on their relevance to respiratory infections. It includes a nanorod-based biosensor suitable for the sensitive and selective detection of biomolecules associated with respiratory infections [20],SpO_2 sensor, a temperature and heart rate detection sensor for vital measurement [21], and an audio sensor to capture and transmit subtle nuances of lung sounds [22]. The raw data acquired from the sense module is transmitted to the core module for subsequent processing. This transfer facilitates further analysis and interpretation of the collected information.

3.2.0.0.2 Core Module : The core module (Fig. 3.1(b)) , comprised of a microcontroller unit (MCU), wireless transmitter, power management unit (PMU), and display unit, collaboratively orchestrates RESPIRE device's functionality. The MCU acts as a central data hub, capturing and processing information from the sense module. Notably, the MCU processes audio data, transmitting it to a cloud-hosted CNN model for lung sound classification. By combining data from vital sensors and biosensors, the MCU gives information on the presence or absence of respiratory disease. The PMU, equipped with a lithium polymer (LiPo) battery and efficiently managed by a Power Management Integrated Circuit (PMIC) and a low-dropout (LDO) voltage regulator, powers up RESPIRE device. An OLED screen and push buttons are added to give user-friendly interface.

3.3 Electrochemical Bio detection

Respiratory diseases like pneumonia, whooping cough, Respiratory Syncytial Virus (RSV) infection caused by various bacteria or viruses[16]. These diseases can be detected using various biosensing techniques, such as Polymerase Chain Reaction (PCR), Surface Plasmonic Resonance (SPR), and Antibody-based electrochemical sensors[5, 6, 7]. Among the different techniques, electrochemical sensors boast affordability, user-friendly operation, portability, and swift detection capabilities. Electrochemical biosensors utilize the interaction between an electrochemical transducer (probe) and biological analytes such as proteins, DNA, or microorganisms to observe impedance changes. One of the detection methods, Electrochemical Impedance Spectroscopy (EIS), enables us to get the target's impedance at different frequencies with a single scan[8]. Typically, EIS is performed using a 3-electrode system, which is simplified using an Interdigitated electrode (IDE) to make it more suitable for point-of-care applications[9]. Interdigitated electrodes (IDEs) integrated with metal oxide nanoparticles have been found to promote chemical interactions and enhance biosensor sensitivity. This is due to the high surface-to-volume ratio of the metal oxides. Among the various metal oxides, zinc oxide (ZnO) is particularly advantageous due to its high sensitivity and ease of customization for specific bacterial detection[10, 11]. The impedance of ZnO nanorod-based sensors changes when bacteria are present in the solution. The shift in impedance indicating the bacterial presence or absence for different respiratory disease. Details on fabrication and characterization of ZnO nanorod based IDE is explained in previous chapter. Also immobilization of any respiratory disease specific antibodies onto ZnO nanorods-based sensors significantly enhances the platform's specificity, thereby facilitating the accurate detection and identification of *Streptococcus pneumoniae*. Upon antigen binding to the antibodies, a change in impedance occurs across the surface, which can be detected using the Electrochemical Impedance Spectroscopy (EIS) method.

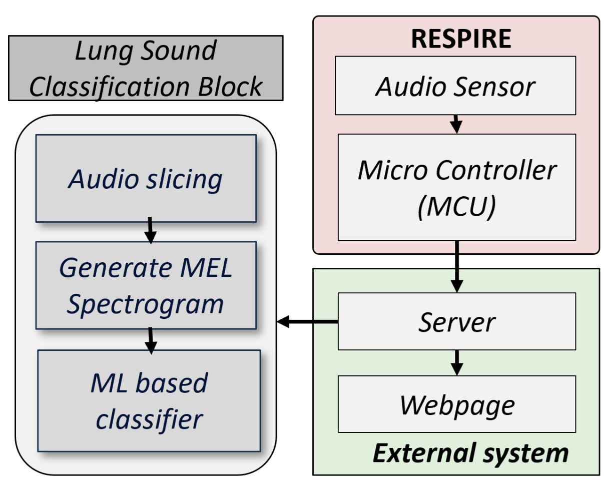

Figure 3.2: Block diagram representation of lung sound classification flow[23]

Table 3.1: Characteristics and frequency Ranges of different lung sounds

Lung sound types	**Frequency (Hz)**
Tracheal breath sounds	100-1000
Bronchial breath sounds	100-800
Bronchovesicular breath sounds	100-700
Vesicular breath sounds	50-150
Crackles	High pitched (fine - 650Hz) / Low pitched (coarse - 350Hz)
Wheezes	>400
Rhonchi	<200

Table 3.2: Vitals for healthy and unhealthy patients

Child Type	**Heart Rate (bpm)**	**SpO_2 Level**
Healthy Child	113	97-99%
Infected Child	120-190	<90%

Table 3.3: Performance Summary of RESPIRE device

Performance Metric	**Value**
Accuracy (lung sound classification)	80.55%
Sensitivity (lung sound classification)	95.65%
Specificity (lung sound classification)	98.8%
SpO_2 Accuracy	$>$ 98%
Temperature Accuracy	$>$ 98%
EIS Error Rate	<15%
Cost	$<$ \$80
Power Consumption	0.788W
Measurement and Processing Time	125s
Weight	$<$ 130g
Dimensions	9.5 cm × 7.3 cm × 3.4 cm
ROM usage	$<$ 1 MB

3.4 Audio Sensing, Classification and Vital Signs Integration

Lung sound plays a pivotal role in detecting respiratory diseases, serving as a key parameter for diagnosis [24, 25]. Particularly in regions with limited access to advanced diagnostic tools like ultrasound, auscultation remains indispensable for initial diagnosis. This section introduces a portable system implemented for classifying respiratory sounds through audio processing and convolutional neural networks (CNN) on mobile platforms. This aids the auscultation process, enabling faster and more accurate diagnoses even in the absence of trained medical professionals and advanced diagnostic equipment. Fig. 3.2 illustrates the block diagram representation of the lung sound classification where RESPIRE device utilizes microcontroller unit to directly capture lung sound data from patients. This data is then transmitted to an IoT cloud server for detailed analysis. Within the cloud service, convolutional neural networks (CNNs) are leveraged for the analysis and classification of recorded respiratory sounds, owing to their exceptional pattern recognition capabilities [23]. The data are then sent to a webpage created for doctors for further analysis.

In this work, along with lung sound classification, other vital signs such as heart rate, SpO_2, and temperature measurements are integrated. Table 3.2 [26, 27, 28, 29] provides potential heart rate and SpO_2 values for healthy and unhealthy individuals. Additionally, unhealthy individuals typically exhibit a temperature elevation exceeding 37.8 °C (100 °F). Data collected from all integrated sensors are transferred wirelessly to a webpage through a WiFi connection. The device also features a user-friendly OLED interface to display results. Along with its lightweight design and fast processing time, the integrated device incorporates a rechargeable battery feature, making it portable.

3.5 Hardware Implementation

In this research as illustrated in Fig.3.3 hardware system for detecting respiratory disease was developed utilizing the ESP32 microcontroller as the main processing unit [30]. The ESP32, known for its low power consumption, high performance, and built-in bluetooth and WiFi capabilities, was chosen for its versatility and suitability for healthcare applications. To ensure accurate measurement of blood oxygen saturation levels, the system employed the AFE4400 Protocentral integrated circuit (IC) connected to the ESP32 microcontroller [31]. Coordinating the pulse oximeter, the ESP32 adeptly collected and processed data from the sensor using SPI protocol. Addressing the challenge of interfacing, a DB-9 connector bridged the ESP32 to a probe on the patient's finger, ensuring a robust and dependable connection. The ubiquity of DB-9 connectors, often Nellcor-based, solidifies its standing as a reliable interfacing method for commercial pulse oximeter probes. In addition to the blood oxygen saturation module, a TMP114 digital temperature sensor from Texas Instruments enhanced the system's capabilities [32]. With its 12-bit resolution, a temperature range spanning from -40 to +125°C, and a meager power consumption of 150 μA, the TMP114 communicated with the ESP32 via the I^2C protocol. Notably, the TMP114 provided superior accuracy compared to infrared sensors available in the market.

The SPI and I^{2}C protocols employ a master-slave architecture to ensure seamless data transfer. In SPI, the master device controls the clock and initiates data transfers, with slave devices responding accordingly. Similarly, in I^{2}C, the master device generates the clock signal and initiates data transfers, while slave devices await commands. This architecture enables straightforward and efficient communication, preventing clashes in data transfer. Additionally, SPI assigns each slave device its own slave select line, while I^{2}C utilizes unique address wires for each device, further enhancing communication reliability.

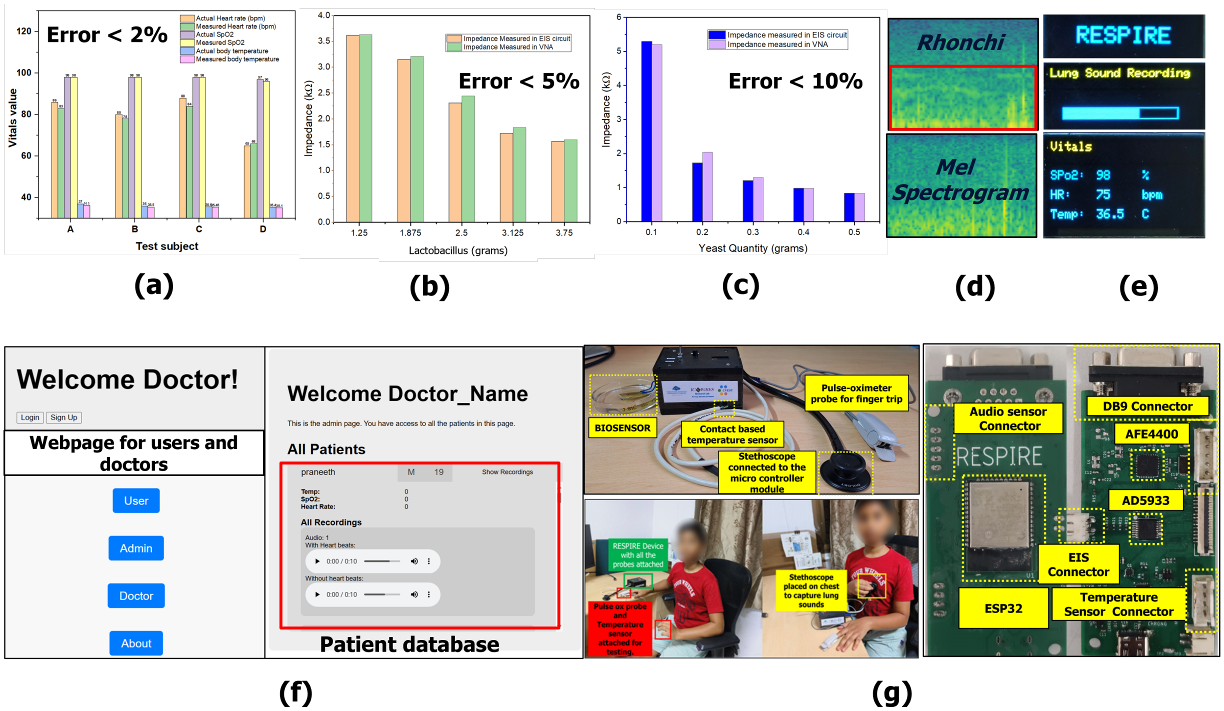

Figure 3.3: Device Outcomes (a) Vitals measurement (b) EIS results for lactobacillus (c) EIS results for yeast (d) Mel spectrogram for classified lung sound (e) OLED results (f) Webpage (g) RESPIRE prototype, PCB, Experimental setup

For audio input, an INMP441 high-performance, low-power digital microphone by InvenSense was seamlessly integrated, operating under the I2S protocol [33]. This microphone, designed to capture high-quality audio across a spectrum of applications, contributed to the system's proficiency in recording lung sounds. The INMP441, responsible for capturing lung sound data, transmitted this invaluable information to a server for subsequent analysis of lung sound types. A ZnO nanorod sensor, gauging impedance, played a pivotal role in discerning the gram-positive or gram-negative nature of pathogens. The AD5933 IC facilitated the measurement of impedance [34]. Components in RESPIRE device chosen in such a way that communication protocol of chosen device is compatible with ESP32.

Equipped with storage functionality, the prototype stored all subject-related data in a dedicated memory storage unit, connected to the MCU via the SPI protocol. This stored data could then be harnessed for further processing, aiding in the prediction of respiratory infection probabilities. Enhancing user experience, the prototype featured an OLED display conveying the device status and the subject's vital data. The OLED display, linked to the MCU through the I^2C protocol, was complemented by basic button controls facilitating device power management and vital monitoring initiation and accessing.

In RESPIRE Device, Power Management Units (PMUs) assumed a pivotal role in efficiently regulating power supply to the electronic systems. For battery safety and longevity, a lithium-ion battery protection IC like DW01 was employed [35]. Additionally, the inclusion of a low-dropout voltage regulator such as FS085 ensured stable voltage regulation [36], with the TLV 3.3 serving as a reliable source for maintaining a consistent 3.3V supply . This intricate interplay of components formed a robust PMU, safeguarding the battery against overcharging, over-discharging, over-current, and short circuits. Also to provide a device with rechargeable feature TP4056 IC is used. Collectively, this combination was indispensable for the reliable and efficient operation of RESPIRE device. Both UART and USB-C ports are available in the device to provide programming capabilities. The total estimated expenditure for fabricating a single unit of RESPIRE device is approximately ***less than $80***. This figure encompasses all essential components, including the costs of electronic components, the manufacturing of the printed circuit board (PCB), and the design and production of a custom 3D-printed enclosure.

3.6 Experimental Results

In our research, the quality of ZnO nanorods was tested using yeast and *Lactobacillus* samples. This approach is supported by the literature, as evidenced by the use of ZnO nanorods for the detection of bacterial pathogens such as *Escherichia coli* and *Staphylococcus aureus* [37]. This method of testing the quality of nanorods is a common practice in the development of biosensors and nanomaterial-based detection systems. The EIS circuit integrated into RESPIRE device underwent rigorous testing with yeast and *Lactobacillus* samples at IIIT Hyderabad lab. Results are summarized in Fig. 3.3(b) and Fig. 3.3(c), demonstrating accuracy with an observed error below 5%. The output of ZnO nanorod-based biosensors showed a concentration-dependent response, with an increase in bacterial concentration correlating with a decrease in impedance. For EIS experiments, the 10–100 kHz frequency range was considered in our test setup. Fig. 3.3(d) shows mel spectrograms results for lung sound classification. The process involves audio recording through the user interface, mel spectrogram generation with noise filtering and heartbeat removal, culminating in effective lung sound classification. Real-time SpO_2, temperature, and heart rate readings from RESPIRE device are displayed on an OLED screen (Fig. 3.3(e)), providing immediate access to vital physiological metrics. Fig. 3.3(a) shows the comparison of measured SpO_2, temperature, and heart rate through RESPIRE device and commercially available devices, demonstrating good accuracy. The entire circuit was supplied with a 4V supply from a Lithium-ion Polymer (LiPo) rechargeable battery and recorded a current consumption of 0.194A with all probes and 0.032A under idle conditions during testing. Fig. 3.3(f) displays a webpage created for doctors containing patient details with all recorded vital values. This helps doctors analyze patient conditions before reaching the hospital. The developed prototype of RESPIRE device, the patient test setup, and the custom-designed PCB with dimensions of 40mm x 78mm made for the device are shown in Fig. 3.3(g). Table.3.3 shows the summary of RESPIRE device performance. RESPIRE device represents a scalable model integrating diverse vital signs and biomarkers. Its modular design facilitates easy expansion to incorporate additional features, ensuring adaptability to evolving research and clinical demands.

3.7 Conclusion

The development of a rechargeable, lightweight, battery-operated device with a user-friendly interface, wireless connectivity, and portability has been successfully achieved. This innovative device, estimated to cost less than $80, represents a significant advancement in the field of portable health monitoring. Consuming a mere 0.788W of power, it is designed to be highly energy-efficient, making it ideal for continuous usage without frequent recharging. Despite its compact size, the device offers robust functionality, integrating multiple health monitoring features that ensure comprehensive diagnostic capabilities.

The device features a quick measurement and processing time of 125 seconds, meeting the demands for swift diagnostic procedures and reducing patient wait times. This speed is particularly advantageous in clinical settings where time is of the essence. Its lightweight design and small dimensions further enhance its portability, making it suitable for on-the-go applications such as home health monitoring, remote medical camps, and emergency medical services.

Quantitative assessments underscore the device's effectiveness, revealing impressive accuracy rates across various parameters. Specifically, the device achieves an accuracy of 80.55% for lung sound classification, which is critical for diagnosing respiratory conditions. It also boasts a sensitivity of 95.65% and a specificity of 98.8%, ensuring that it reliably detects true positives while minimizing false positives. Additionally, the device's measurements for blood oxygen saturation (SpO_2) and temperature exceed the 98% accuracy mark, providing reliable vital signs monitoring.

The integration of Electrical Impedance Spectroscopy (EIS) into the device further enhances its diagnostic capabilities. EIS has demonstrated an error rate of less than 15% for detecting 0.02 grams of yeast in 20 ml (20.9 x 10^6 cells/ml), emphasizing the device's precision and reliability in biochemical analyses. This feature makes the device versatile, extending its applications beyond respiratory health to include other diagnostic areas.

Notably, the device stands out for its affordability, making advanced health monitoring accessible to a broader population. Its low power consumption ensures extended use, while its modular design allows for easy upgrades and customization to cater to diverse user needs. The exceptional accuracy and efficient resource utilization on an embedded platform reinforce the device's utility in various healthcare settings, from hospitals to remote clinics.

In essence, this research advances the frontier of medical diagnostics, offering a cost-effective, low-power solution with high accuracy and versatility. As a device designed to detect respiratory diseases, it promises to significantly impact the landscape of portable health monitoring devices. By providing accessible and reliable healthcare solutions to individuals worldwide, this device holds the potential to improve health outcomes and enhance the quality of life for many.

Chapter 4

Design and Analysis of Active High Pass Filter Topology for Low-Frequency Noise suppression in Signal Processing Applications

4.1 Introduction

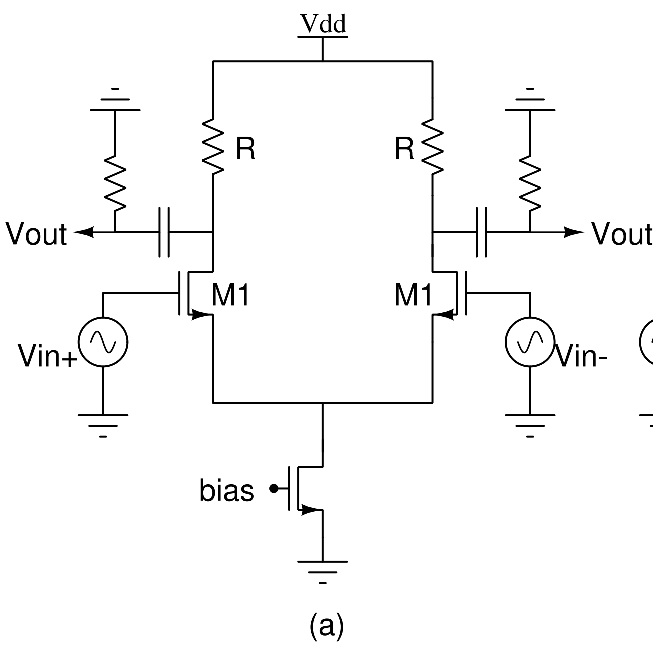

Figure 4.1: (a) Resistor load based Active high pass filter without source degeneration (b) Active load-based source degenerated high pass filter with source degeneration [38]

The effective operation of communication and signal processing systems hinges on the ability to alleviate challenges such as spillover and low-frequency unwanted signals. Spillover, characterized by the undesired leakage or interference of signals from one frequency band to another, poses a significant threat to system performance, leading to spectral regrowth and interference in adjacent frequency bands.

Meanwhile, low-frequency unwanted signals, arising from sources like thermal noise, DC offsets, and external interference, introduce additional complexities to receiver circuits, potentially degrading signal fidelity and system reliability. To address these challenges, filtering of low-frequency signals becomes imperative. Active high pass filters are preferred over passive filters to tackle this issue, owing to their ability to provide amplification, minimize pass band energy loss, and avoid load effects, thereby offering enhanced performance and versatility across various applications[39].

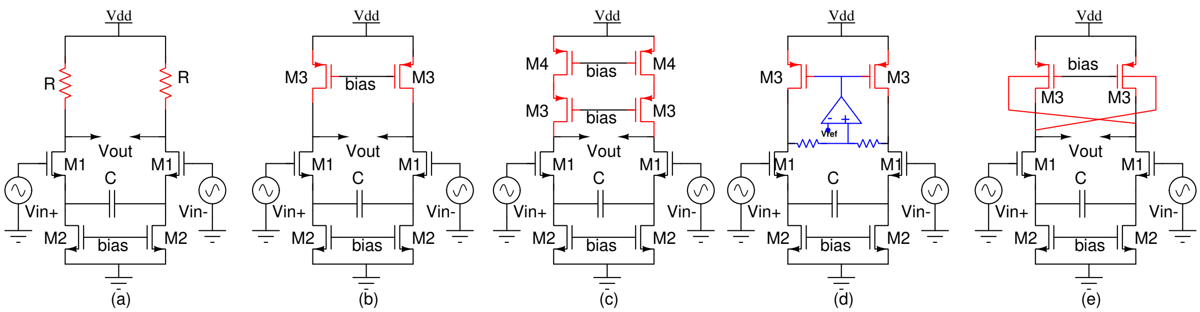

Figure 4.2: (a) Resistor load-based source degenerated high pass filter (b) Active load-based source degenerated high pass filter (c) cascode load-based source degenerated high pass filter (d)Modified active load-based source degenerated high pass filter with CMFB (e) Body cross coupled mosfet load-based source degenerated high pass filter

Table 4.1: Different topology voltage gain comparison

Topology	Fig. 2(a)	Fig. 2(b)	Fig. 2(c)	Fig. 2(e)
Gain (Av)	$Av = -\frac{gm1 \cdot R}{1 + gm1 \cdot Zs}$ $Z_s = \frac{ro2}{1 + sC \cdot ro2}$	$Av = -\frac{gm1 \cdot ro3}{1 + gm1 \cdot Zs}$ $Z_s = \frac{ro2}{1 + sC \cdot ro2}$	$Av = -\frac{gm1 \cdot Reff}{1 + gm1 \cdot Zs}$ $Z_s = \frac{ro2}{1 + sC \cdot ro2}$	$Av = -\frac{gm1 \cdot Reff}{1 + gm1 \cdot Zs}$ $Z_s = \frac{ro2}{1 + sC \cdot ro2}$
Output Resistance (Reff)	Reff = R	Reff = ro3	Reff = $(gm3 \cdot ro3 \cdot ro4) \parallel (gm1 \cdot ro1 \cdot ro2)$	$R_{\text{eff}} = \frac{1}{g_{mb}}$

This work introduces various high pass filter topologies aimed at mitigating low-frequency interference in baseband chains. Leveraging the benefits of low power and the superior linearity of source degeneration circuits, we propose an active high pass filter topology implemented using TSMC 65 nm CMOS technology. Post-layout simulation results validate its efficacy, highlighting its potential for seamless integration into receiver baseband chains. The subsequent sections are structured as follows: Section 4.2 offers an overview of the advantages of source degeneration over non-degenerated differential amplifiers. Sections 4.3 and 4.4 address design challenges and propose a novel topology to overcome them. Section 4.5 presents a detailed analysis of the obtained results, encompassing both pre-layout and post-layout assessments. Finally, Section 4.6 concludes the work by summarizing key findings and their implications.

4.2 Advantages of Source Degenerated Active HPF

Fig. 4.1 illustrates two configurations of active high pass filters: one with a resistor load-based non-source degenerated amplifier (Fig. 4.1(a)), and the other with a source degenerated amplifier (Fig. 4.1(b)). The use of the source degenerated configuration (Fig. 4.1(b)) reduces power consumption compared to a conventional amplifier by increasing output impedance, thus lowering transconductance and gain, resulting in reduced power dissipation. It also enhances linearity by mitigating variations in transistor transconductance (g_m), ensuring a more constant gain. This reduction in gain variation leads to a more linear amplifier, improving output waveform fidelity and reducing distortion. Linearity for half circuit is quantified by the third-order input intercept point (IIP3), expressed as[40]:

$$\text{IIP3} = \sqrt{\frac{2g_{m1}}{3Z_s}} \cdot \frac{(1 + g_{m1}Z_s)^2}{K} \tag{4.1}$$

where $K = \frac{1}{2} \cdot \mu_n \cdot C_{ox} \cdot \left(\frac{W}{L}\right)$, g_{m1} represents transconductance, and Z_s, R_L, μ_n, and C_{ox} denote source degenerated impedance, load resistance, mobility, and oxide capacitance respectively. Increasing Z_s and the amplifier's intrinsic gain enhances linearity despite the decreased total gain due to source degeneration, as shown in Eq. 4.2.

$$A_v = -\frac{g_m \cdot R}{1 + g_m \cdot Z_s}, \quad \text{where } Z_s = ro || \frac{1}{s \cdot (2C)}. \tag{4.2}$$

In the proposed design, active high pass filters with source degeneration are designed considering their advantages, including reduced power consumption and improved linearity, making them preferable in applications such as high-fidelity audio amplification and sensor interfaces, where superior linearity and stability are critical for accurate signal processing and reproduction.

4.3 Design Challenges

The zero and pole equations for the circuit depicted in Fig. 4.1(b) are defined as follows [38]:

$$f_Z = \frac{1}{2\pi C_s R_s} \tag{4.3}$$

$$f_H = -\frac{(R_L + r_o + R_s + g_m r_o R_s)}{2\pi C_s R_s (R_L + r_o)} \tag{4.4}$$

where C_s represents the source capacitance, calculated as Cs = 2C. A primary challenge in designing for a lower cutoff frequency in this circuit is the necessity to increase either the source capacitance C_s or the load resistance. However, both approaches present drawbacks. Increasing the load resistance leads to higher power dissipation, larger voltage drops across the load, potentially causing signal clipping or distortion, and a larger layout area. Conversely, increasing the capacitance introduces phase shift in the amplifier's frequency response. This phase shift can distort the output signal, particularly at higher frequencies, leading to waveform distortion and signal degradation, it may introduce oscillations or instability issues in the circuit, and limit the amplifier's slew rate.

We propose a new active without feedback that is open-loop HPF topology that eliminates the drawbacks associated with traditional approaches. The key innovation lies in replacing the resistance with a MOSFET-based configuration, offering advantages such as high input impedance, low output impedance, and minimal loading effects on preceding stages. Additionally, it provides variable impedance control and low static power consumption, making it suitable for high-performance circuits requiring dynamic load adjustments and enabling compact and highly integrated designs. However, MOSFET non-linearity, increased flicker noise, and biasing requirements must be considered when selecting and implementing a MOSFET-based solution [40]. This study aims to overcome the limitations of existing designs, particularly power, noise and area constraints, and offers a more efficient and effective solution for lower cutoff frequency design challenges.

4.4 Proposed HPF Topology

To tackle the design challenges outlined in Section 4.3, the resistor load in the differential amplifier is replaced with a MOSFET-based current source [40], as depicted in Fig. 4.2(b). This modification ensures that the maximum impedance at the load is the small-signal output resistance (r_o), which is kept low to achieve a low frequency. To further bolster this impedance, cascode MOSFET loads are introduced, as shown in Fig. 4.2(c). Although this topology effectively achieves a high cutoff frequency, it introduces a potential issue by necessitating more than one current source. Incorporating multiple current sources in operational transconductance amplifiers (OTAs) poses a significant challenge due to the inherent risk of current mismatch, leading to variations in the common-mode voltage. Such discrepancies in currents impact the balance of the differential input stage, resulting in undesirable shifts in the operating point and potential degradation of performance parameters such as linearity and dynamic range. To ease this challenge, robust common-mode feedback (CMFB) mechanisms are integrated, as depicted in Fig. 4.2(d), ensuring precise control over the common-mode voltage and guaranteeing stable OTA operation across various operating and load conditions [41]. However, this addition leads to increased power dissipation, circuit complexity, and noise. New topology the bulk cross-coupled constant gate-biased load as illustrated in Fig. 4.2(e), is introduced [42] to achieve lower cutoff frequency. But this solution introduces a new challenge associated with positive feedback due to the bulk connection and body effects [42],[43] thereby enhancing sensitivity to process variations and mismatch, potentially leading to variations in the biasing conditions of the transistors and adversely affecting amplifier performance and stability. The voltage gain equations for these topologies are provided in table 4.1. To further tackle these issues, we propose the integration of gate cross-coupled with a diode load in the source-degenerated active filter, as illustrated in Fig. 4.3(a), aiming to achieve low power, low noise, lower cutoff frequency, and moderate linearity.

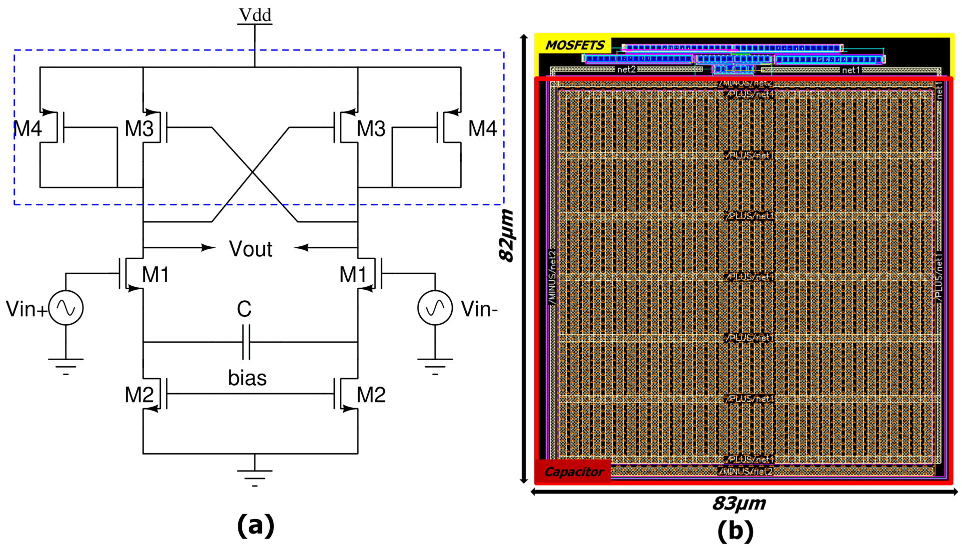

Figure 4.3: (a) Schematic of proposed cross-coupled with diode-connected load-based active HPF (b) Layout

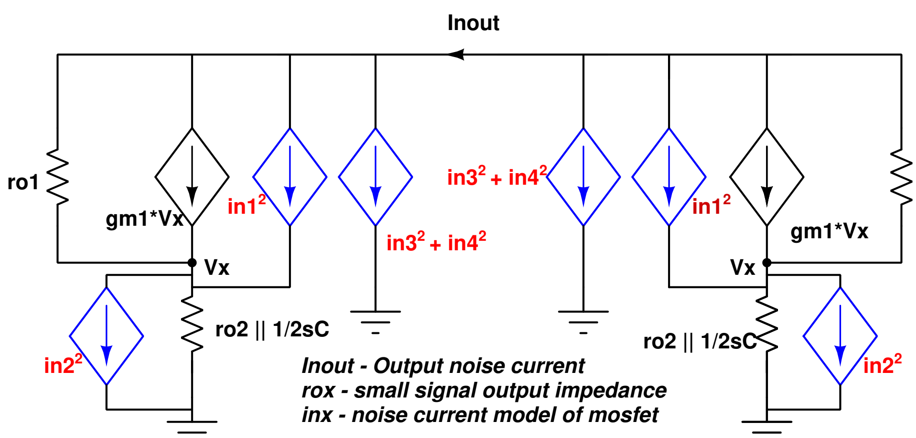

Figure 4.4: Noise model for Fig. 4.3 (a)

The gain equation for this topology is derived from Eq. 4.2, where R and Z_s are replaced by $\frac{1}{g_{m4}-g_{m3}}$ and $r_{o2}||\frac{1}{sC}$ respectively. The zero and pole frequencies for this design are approximately $\frac{1}{r_o} \times \frac{1}{C}$ and $\frac{1}{\left(\frac{1}{g_{m4}-g_{m3}}||g_{m1}\cdot r_{o1}\cdot r_{o2}\right)}\frac{1}{C}$ respectively. Fig.4.4 shows the output short-circuited noise current model for the proposed topology with high r_o. The output noise current density equation is given as:

$$I_{n_{out}}^2 = 2 \cdot I_{n_1}^2 + \frac{I_{n_3}^2}{2} + \frac{I_{n_4}^2}{2} \tag{4.5}$$

where $i_{nx}^2 = 4K\top\gamma g_{mx} + g_{mx}^2 \cdot \frac{k}{\omega LC_{0x}} \cdot 1/f$.

The input-referred noise voltage is given as: cc

$$\overline{V_{n,\text{ in}}^2} = \frac{\overline{I_{n\text{out}}^2}}{G_{\text{meff}}^2} \tag{4.6}$$

where $G_{\text{meff}} = \frac{g_{m1}}{1+g_{m1}\text{Zs}}$. Compared to other topologies, this circuit offers lower noise since the total output noise current is $4 \cdot I_{nx}^2$ if noise current density from all transistors is equal in other topology.

4.5 Results

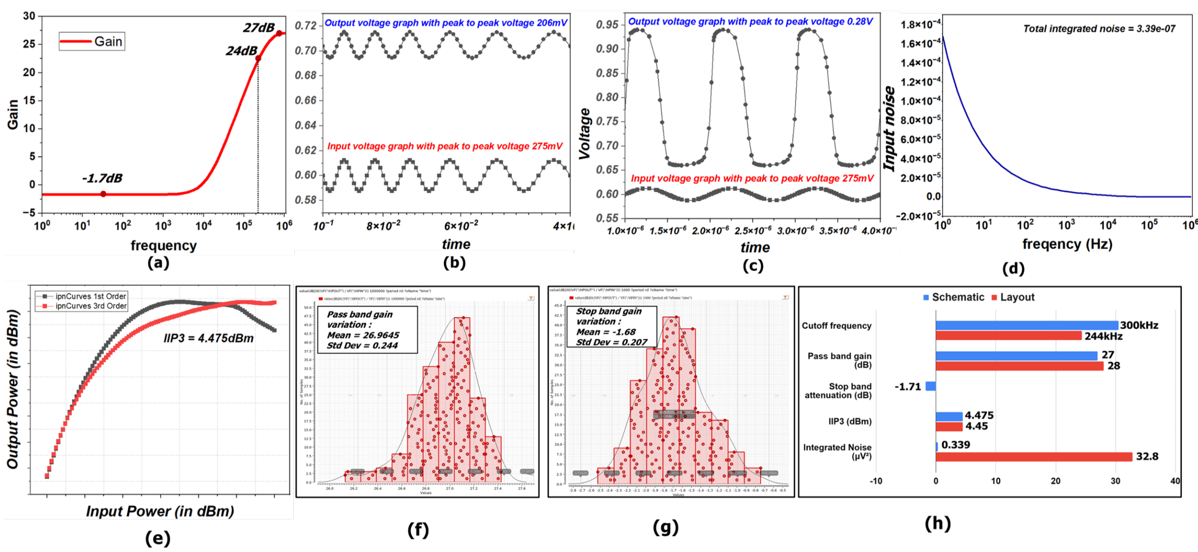

Figure 4.5: (a) AC gain (b) Low frequency transient (c) High frequency transient (d) Input noise (e) IIP3 (f) Monte Carlo for pass band gain (g) Monte Carlo for stop band gain (h) Pre and post layout comparison

Table 4.2: Comparison of different proposed topologies

Topology Used	Pass band Voltage Gain (dB)	Stop band Voltage Gain (dB)	Cutoff Frequency (kHz)	Capacitance Value (pF)	IIP3 (dBm)	Integrated Noise (V^2)	Power Consumption (µW)
Fig 2a	4.18	-31.36	298	20.2	3.74	0.358	9.752 µW
Fig 2b	30.83	-1.69	307	20.2	6.65	19.85	20.16 µW
Fig 2e	27.26	-8.754	313	20.2	4.645	6.379×10^{-7}	9.67 µW
Fig 3	27	-1.71	305	12	4.475	3.39×10^{-7}	12.97 µW

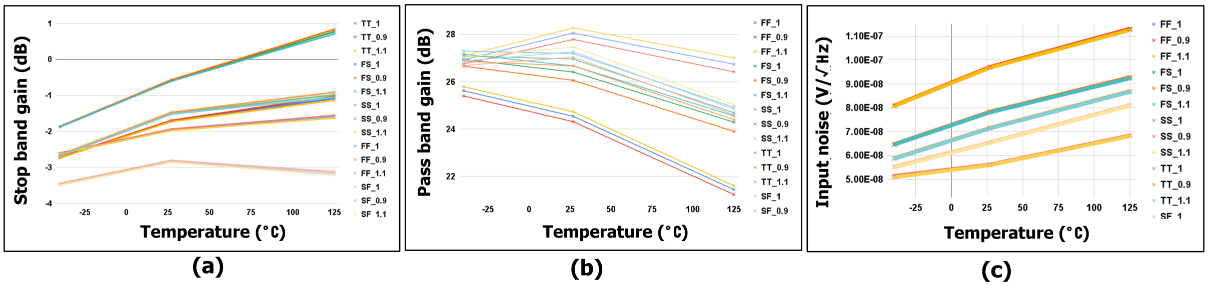

Figure 4.6: (a) Stopband gain (b) Passband gain (c) Input refereed noise at cut off frequency at various PVT corners

Fig. 4.3(a) illustrates the final implemented design of the proposed active filter topology in TSMC 65 nm. A MOSFET-based source degeneration technique is employed over a resistor to mitigate thermal noise emanating from the resistor. In this implemented topology, a capacitance of 12pF is selected to attain a cutoff frequency of 300 kHz. This choice of cutoff frequency is informed by the requirements of the analog baseband in FMCW radar applications, where the spillover frequency is contingent upon the chirp time[44]. Considering a bandwidth (B) of 4 GHz, a distance (x) of 10 meters, and an Intermediate Frequency (IF) bandwidth of 10 MHz, the chip frequency is approximated to be 37 kHz by substituting these values into the equation: $IF = \frac{B \cdot 2x}{t_c \cdot c}$. The designed filter draws a current of 12.97 μA from a 1 V supply. Fig. 4.5(a) shows an AC analysis plot with achieved 27 dB passband gain and -1.7 dB stop band gain, exhibiting a slope of 20 dB/decade. Fig. 4.5(b) and Fig. 4.5(c) represent transient results at Vout and Vin+ for low frequency and high frequency, respectively, demonstrating the functionality of the designed filter. Fig. 4.5(d) represents the input noise plot, with MOSFET flicker noise dominating in this design. The achieved total integrated noise of the design is 0.39 μV^2 over 10MHz bandwidth.

The linearity plot is shown in Fig. 4.5(e) with an achieved IIP3 of 4.475 dBm indicates design achieves moderate linearity compared to other designs. Monte Carlo analysis is conducted on the design to check the variation of pass band and stop band gain, as shown in Fig. 4.5(f) and Fig. 4.5(g). The mean value obtained for the pass band and stop band is 26.9 dB and -1.68 dB, respectively, indicating lesser variation and thus the reliability of the device to mismatches.

Fig. 4.3(b) shows the layout of Fig. 4.3 designed in TSMC 65 nm. Mimcaps are used in the design, and the total layout area is 83μm x 82 μm. Pre- and post-layout performance comparison is provided in Fig. 4.5(g). Figure 4.6 illustrates the PVT corners results of the proposed design, demonstrating reduced sensitivity to variations in process, voltage, and temperature. Table 4.2 gives comparison of simulation results of different topologies mentioned in this work. It shows that the proposed topology achieves low noise, low power, good linearity, and lesser layout area compared to other topologies.

4.6 Conclusion

This research work addresses the challenges associated with different active open-loop high-pass filter topologies and proposes a novel cross-coupled configuration with a diode-connected load to overcome these challenges. The design is realized using CMOS TSMC 65 nm technology, which offers a promising solution for high-performance filter applications.

The simulation results of the proposed filter reveal several key performance metrics. Notably, the filter achieves a cutoff frequency of 300 kHz, ensuring effective high-pass filtering for a wide range of applications. Additionally, the passband gain is measured at 27 dB, indicating significant signal amplification within the desired frequency range. The input third-order intercept point (IIP3) is determined to be 4.475 dBm, reflecting the filter's strong linearity and its capability to handle high signal levels without significant distortion. The integrated noise level is quantified at 3.39×10^{-7} V^2, underscoring the design's low-noise characteristics which are crucial for maintaining signal integrity in sensitive applications.

Moreover, the filter demonstrates a power consumption of 12.97 μW, operating efficiently from a 1 V supply. This low power requirement is particularly advantageous for battery-powered and portable electronic devices, where power efficiency is a critical parameter.

The combination of these performance metrics—high cutoff frequency, substantial passband gain, excellent linearity, low noise, and low power consumption—illustrates the effectiveness and viability of the proposed design. Compared to other designs, this filter topology offers superior performance, making it a highly attractive option for various high-performance filtering applications in modern electronic systems.

Overall, the innovative cross-coupled configuration with a diode-connected load not only addresses the limitations of existing high-pass filter topologies but also sets a new benchmark for performance in CMOS technology. Future research may further optimize and adapt this design for specific applications, potentially exploring scalability and integration with other circuit components to enhance functionality and efficiency in comprehensive electronic systems.

Chapter 5

Conclusions and Future Work

5.1 Research Contributions

In conclusion, this thesis has made significant strides in advancing healthcare technology, particularly in the fields of point-of-care (POC) diagnostics and biosensing. Through the development and implementation of innovative technologies, as well as the design and testing of practical and portable systems, several key advancements have been achieved.

The research contributions of this thesis can be summarized as follows:

Development and Implementation of a Biosensor Circuit: The thesis introduces a novel biosensor design, fabrication, and circuit utilizing Electrochemical Impedance Spectroscopy (EIS), specifically optimized for healthcare applications. By successfully testing this circuit with biological samples such as yeast and lactobacillus using a gold Interdigitated Electrode (IDE) biosensor, a robust platform for real-time and label-free detection of biological analytes has been established.

Key contributions include:

1. Design and fabrication of the biosensor PCB

2. Rigorous testing and validation of biosensor performance

Healthcare System for Respiratory Disease Detection (RESPIRE): The thesis details the design and testing of RESPIRE, a low-cost and portable integrated system capable of 'Go/No-Go' assessments. By integrating various sensors within a cohesive unit and fabricating associated printed circuit boards (PCBs) and 3D-printed enclosures, RESPIRE offers a practical solution for rapid and accurate point-of-care (POC) diagnostics, particularly in the realm of respiratory health.

Key contributions include:

1. Development and testing of RESPIRE prototype

2. Conducting comprehensive clinical trials to evaluate system performance

Innovative Design of a Low-Frequency Active High Pass Filter: Additionally, the thesis presents an innovative low-frequency active high pass filter design. By exploring various topologies and providing comparative performance results, this novel filter design addresses challenges such as spillover and low-frequency unwanted signals, thereby offering enhanced performance and versatility across multiple applications.

Key contributions include:

1. Design and optimization of the high pass filter circuit

2. Thorough pre and post-layout testing to validate filter performance

In conclusion, the research presented in this thesis represents a significant step forward in the development of advanced biosensing technologies and POC diagnostic devices. These innovations have the potential to revolutionize healthcare delivery by enabling rapid, accurate, and accessible diagnostics, ultimately improving patient outcomes and advancing the field of medical technology.

5.2 Future Works

To enhance the functionality and accuracy of the RESPIRE device, several features can be incorporated:

1. Addition of ECG Feature: Integrating an ECG feature alongside existing functionalities in the RESPIRE device can significantly enhance its diagnostic capabilities. ECG data can provide valuable insights into cardiac health, complementing the respiratory parameters measured by the device.

2. Power Failure Detection Feature: Implementing a feature to detect power failures in the RESPIRE device ensures uninterrupted operation and data integrity, especially in critical healthcare scenarios where continuous monitoring is essential.

3. Contactless Temperature, Heart Rate, and SpO_2 Measurement: Developing contactless methods for measuring temperature, heart rate, and SpO_2 levels further enhances the device's usability and convenience for both patients and healthcare professionals.

4. Integration of Digital Stethoscope: Incorporating a digital stethoscope within the RESPIRE device offers additional diagnostic capabilities, allowing for the detection and analysis of lung sounds and abnormalities.

5. Reduction of Biosensor Size: Streamlining the size of the biosensor makes it more practical and market-ready, ensuring ease of use and portability without compromising performance.

6. Disease-Specific Indication: Currently, the RESPIRE device does not provide indications of specific respiratory diseases. Adding features to identify and differentiate between different respiratory conditions can improve diagnostic accuracy and aid in targeted treatment.

On the circuit side, the following optimizations can be made:

1. High Pass Filter Optimization: Further optimization of the developed high pass filter can improve its linearity and reduce noise.
2. Design of Analog Baseband Chain: Implementing an analog baseband chain using the designed active high pass filter enables efficient signal conditioning and processing, ensuring reliable data acquisition and analysis.

Related Publications

Accepted Publications

1. **Deeksha** and A. Srivastava, ”Design and Evaluation of Active High Pass Filter Topologies for Analog Baseband” 2024 Midwest Symposium on Circuits and Systems (MWSCAS), Springfield MA, 2024.
2. A. Sahni*, K.V. Varma*, **Deeksha**, B. Ghosh, A. Sarje, and A. Srivastava, ”Design of Integrated System for Detection of Micro-organisms with Fabrication and Testing of ZnO Nanorods based Biosensor” 2023 IEEE Biomedical Circuits and Systems Conference (BioCAS), Toronto, Canada, 2023 *(*Equal contribution)*
3. Swarnim Sinha, **Deeksha**, Nitin Srinivas, Shiva Sharma ”Flexible Multi-Band Reconfigurable Modified Microstrip Antenna” 2024 Midwest Symposium on Circuits and Systems (MWSCAS), Springfield MA, 2024.

Submitted Manuscript

Deeksha, S. Somachi, K.V. Varma, A. Tripathi, A. Sahni, A.S.Sunil, P.Gokula, M.Pratyusha, G.Bhaswar, A.Sarje and A. Srivastava, ”Enhancing Pediatric Healthcare With RESPIRE: A Portable Low Power Go/No-Go Device for Early-Stage Pneumonia Detection”

Patents

A. Srivastava, B. Ghosh, A. Sarje, **Deeksha**, A. Tripathi, A. Sahni, “A Portable System for Pneumonia Detection using Simultaneous Measurement of Vitals and Artificial Intelligence Capabilities”, Filed Provisional Patent in Indian Patent Office, Application No.:202341044162, June 2023

Bibliography

[1] A Soley et al. “On-line monitoring of yeast cell growth by impedance spectroscopy”. en. In: *J Biotechnol* 118.4 (Sept. 2005), pp. 398–405.

[2] Rashi Borgohain and Sunandan Baruah. “Development and Testing of ZnO Nanorods Based Biosensor on Model Gram-Positive and Gram-Negative Bacteria”. In: *IEEE Sensors Journal* 17.9 (2017), pp. 2649–2653. DOI: 10.1109/JSEN.2017.2682920.

[3] Shruti Jha, Ritu Rani, and Sandeep Singh. “Biogenic Zinc Oxide Nanoparticles and Their Biomedical Applications: A Review”. In: *Journal of Inorganic and Organometallic Polymers and Materials* 33.6 (June 2023), pp. 1437–1452.

[4] Sankush Krishna Maheshuni et al. “A Review on 2D-ZnO Nanostructures Based Biosensors: From Materials to Devices”. In: *Materials Advances* (Nov. 2022). DOI: 10.1039/D2MA00878E.

[5] A. Soley et al. “On-line monitoring of yeast cell growth by impedance spectroscopy.” In: *J Biotechnology* 118.4 (2005), pp. 398–405.

[6] T.M. File and R.S. Kozlov. “Rapid detection of Streptococcus pneumoniae in community-acquired pneumonia”. In: *Clinical Microbiology and Infection* 12 (2006), pp. 27–33. ISSN: 1198-743X. DOI: https://doi.org/10.1111/j.1469-0691.2006.01653.x. URL: https://www.sciencedirect.com/science/article/pii/S1198743X14621352.

[7] Setareh Homayoonnia et al. “Micro/nanotechnology-inspired rapid diagnosis of respiratory infectious diseases”. In: *Biomedical Engineering Letters* (2021), pp. 1–31.

[8] I Jócsák, G Végvári, and E Vozáry. “Electrical impedance measurement on plants: a review with some insights to other fields”. In: *Theoretical and Experimental Plant Physiology* 31 (2019), pp. 359–375. DOI: https://doi.org/10.1007/s40626-019-00152-y.

[9] Aatha Mohin Shaikh et al. "Addressing Non-Idealities and EIS Measurement: From Inspection to Implementation". In: *IEEE Instrumentation Measurement Magazine* 26.9 (2023), pp. 45–52. DOI: 10.1109/MIM.2023.10328669.

[10] Rajesh Kumar et al. "Antimicrobial properties of ZnO nanomaterials: A review". In: *Ceramics International* 43.5 (2017), pp. 3940–3961. ISSN: 0272-8842. DOI: https://doi.org/10.1016/j.ceramint.2016.12.062. URL: https://www.sciencedirect.com/science/article/pii/S0272884216323124.

[11] Nagarajan Padmavathy and Rajagopalan Vijayaraghavan. "Interaction of ZnO nanoparticles with microbes–a physio and biochemical assay". In: *Journal of biomedical nanotechnology* 7.6 (2011), pp. 813–822. DOI: doi:10.1166/jbn.2011.1343.

[12] Arpit Sahni et al. "Design of Integrated System for Detection of Micro-organisms with Fabrication and Testing of ZnO Nanorods based Biosensor". In: *2023 IEEE Artificial Intelligence BioMedical Circuits And Systems For Health (BIOCAS)*. 2023.

[13] R. Borgohain and S. Baruah. "Development and Testing of ZnO Nanorods Based Biosensor on Model Gram-Positive and Gram-Negative Bacteria". In: *IEEE Sensors Journal* 17.9 (2017), pp. 2649–2653. DOI: 10.1109/JSEN.2017.2682920.

[14] Ummar Pasha Shaik et al. "Growth of superhydrophobic Zinc oxide nanowire thin films". In: *Materials Letters* 75 (2012), pp. 51–53. ISSN: 0167-577X. DOI: https://doi.org/10.1016/j.matlet.2012.01.140. URL: https://www.sciencedirect.com/science/article/pii/S0167577X12001826.

[15] Younas Iqbal et al. "Orientation and actual growth mechanism of ZnO nanorods through hydrothermal method on gold seed layer". In: *AIP Advances* 11.12 (Dec. 2021), p. 125006. ISSN: 2158-3226. DOI: 10.1063/5.0067231. URL: https://doi.org/10.1063/5.0067231.

[16] *WHO data*. URL: https://www.who.int/health-topics/chronic-respiratory-diseases#tab=tab_1.

[17] *Global Burden of Disease Study*. URL: url%20=%20%7Bhttps://www.healthdata.org/research-analysis/library/global-burden-chronic-respiratory-diseases-and-risk-factors-1990-2019%7D,.

[18] Persijn Honkoop, Omar Usmani, and Matteo Bonini. “The current and future role of technology in respiratory care”. In: *Pulmonary Therapy* 8.2 (2022), pp. 167–179.

[19] Li Li et al. “Prediction and Diagnosis of respiratory disease by combining convolutional neural network and bi-directional long short-term memory methods”. In: *Frontiers in public health* 10 (2022), p. 881234.

[20] Jinping Wang et al. “Clinically relevant detection of Streptococcus pneumoniae with DNA-antibody nanostructures”. In: *Analytical chemistry* 89.12 (2017), pp. 6900–6906.

[21] Joshua P Metlay and Michael J Fine. “Testing strategies in the initial management of patients with community-acquired pneumonia”. In: *Annals of internal medicine* 138.2 (2003), pp. 109–118.

[22] Raymond LH Murphy et al. “Automated lung sound analysis in patients with pneumonia”. In: *Respiratory care* 49.12 (2004), pp. 1490–1497.

[23] Abhishek Srivastava Adithya Sunil Edakkadan. “Deep Learning Based Portable Respiratory Sound Classification System: An Unpublished Research Paper”. Paper accepted for presentation at the APCCAS 2023 Conference. 2023.

[24] Mohammad Fraiwan et al. “Recognition of pulmonary diseases from lung sounds using convolutional neural networks and long short-term memory”. In: *Journal of Ambient Intelligence and Humanized Computing* (2022), pp. 1–13.

[25] Kumari Nidhi Lal. “A lung sound recognition model to diagnoses the respiratory diseases by using transfer learning”. In: *Multimedia Tools and Applications* 82.23 (2023), pp. 36615–36631.

[26] Susannah Fleming et al. “Normal ranges of heart rate and respiratory rate in children from birth to 18 years of age: a systematic review of observational studies”. en. In: *Lancet* 377.9770 (Mar. 2011), pp. 1011–1018.

[27] Monica K Mau, Kelly S Yamasato, and Loren G Yamamoto. “Normal oxygen saturation values in pediatric patients”. en. In: *Hawaii Med J* 64.2 (Feb. 2005), pp. 42, 44–5.

[28] Eric D McCollum et al. “Pulse oximetry for children with pneumonia treated as outpatients in rural Malawi”. en. In: *Bull World Health Organ* 94.12 (Oct. 2016), pp. 893–902.

[29] Wanli Li et al. “Emergency treatment and nursing of children with severe pneumonia complicated by heart failure and respiratory failure: 10 case reports”. en. In: *Exp Ther Med* 12.4 (July 2016), pp. 2145–2149.

[30] *ESP 32 datasheet*. URL: https://pdf1.alldatasheet.com/datasheet-pdf/view/1243003/ESPRESSIF/ESP32.html.

[31] *AFE4490 datasheet*. URL: https://www.ti.com/lit/ds/symlink/afe4490.pdf?HQS=TI-null-null-alldatasheets-df-pf-SEP-wwe&ts=1703311128614&ref_url=https%253A%252F%252Fpdf1.alldatasheet.com%252F.

[32] *TMP114 datasheet*. URL: https://www.ti.com/lit/ds/symlink/tmp114.pdf?HQS=TI-null-null-alldatasheets-df-pf-SEP-wwe&ts=1703311387201&ref_url=https%253A%252F%252Fpdf1.alldatasheet.com%252F.

[33] *INMP441 datasheet*. URL: https://www.alldatasheet.com/view.jsp?Searchword=INMP441&sField=4.

[34] *AD5933 datasheet*. URL: https://pdf1.alldatasheet.com/datasheet-pdf/view/99319/AD/AD5933.html.

[35] *DW01 datasheet*. URL: https://pdf1.alldatasheet.com/datasheet-pdf/view/256691/ETC2/DW01.html.

[36] *FS085 datasheet*. URL: https://www.alldatasheet.com/view.jsp?Searchword=FS085&sField=1.

[37] Mayuree Jaisai, Sunandan Baruah, and Joydeep Dutta. "Paper modified with ZnO nanorods–antimicrobial studies". In: *Beilstein journal of nanotechnology* 3.1 (2012), pp. 684–691.

[38] Anirudh Praveen Kankuppe Raghavendra Swamy et al. "A Wideband 62-mW 60-GHz FMCW Radar in 28-nm CMOS". In: (2021).

[39] Sharil Nivitha Rodrigues and PS Sushma. "Design of Low-Power Active High-Pass Filter Using Operational Transconductance Amplifier". In: *Advances in Communication, Signal Processing, VLSI, and Embedded Systems: Select Proceedings of VSPICE 2019*. Springer. 2020, pp. 39–54.

[40] Behzad Razavi. *Design of analog CMOS integrated circuits*., 2005.

[41] Hung-Yi Lin, Yen-Tai Lai, and Chi-Chou Kao. "A simple scheme to extend the linearity of the continuous-time CMFB circuit for fully-differential amplifier". In: *TENCON 2008-2008 IEEE Region 10 Conference*. IEEE. 2008, pp. 1–4.

[42] Andrea Ballo, Alfio D Grasso, and Salvatore Pennisi. “Active load with cross-coupled bulk for high-gain high-CMRR nanometer CMOS differential stages”. In: *International Journal of Circuit Theory and Applications* 47.10 (2019), pp. 1700–1704.

[43] Dattaguru V Kamat, PV Ananda Mohan, and K Gopalakrishna Prabhu. “Novel first-order and second-order current-mode filters using multiple-output operational transconductance amplifiers”. In: *Circuits, Systems and Signal Processing* 29 (2010), pp. 553–576.

[44] Anirudh Kankuppe et al. “A 67-mW D-band FMCW I/Q radar receiver with an N-path spillover notch filter in 28-nm CMOS”. In: *IEEE Journal of Solid-State Circuits* 57.7 (2022), pp. 1982–1996.